

Analog In-Memory Computing Attention Mechanism for Fast and Energy-Efficient Large Language Models

Nathan Leroux^{1,†}, Paul-Philipp Manea^{2,3,†}, Chirag Sudarshan²,
Jan Finkbeiner^{1,3}, Sebastian Siegel², John Paul Strachan^{2,3},
Emre Neftci^{1,3}

¹ Peter Grünberg Institute 15, Forschungszentrum Jülich, Jülich, Germany

² Peter Grünberg Institute 14, Forschungszentrum Jülich, Jülich, Germany

³ Faculty of Electrical Engineering, RWTH Aachen, Aachen, Germany

[†] Equally contributing authors

E-mail: n.leroux@fz-juelich.de, p.manea@fz-juelich.de

Abstract. Transformer neural networks, driven by self-attention mechanisms, are core components of foundational and Large Language Models. In generative transformers, self-attention uses cache memory to store token projections, avoiding recomputation at each time step. However, GPU-stored projections must be loaded into SRAM for each new generation step, causing latency and energy bottlenecks for long sequences.

In this work, we propose a fast and energy-efficient hardware implementation of self-attention using analog in-memory computing based on gain cell memories. Volatile gain cell memories can be efficiently written to store new tokens during sequence generation, while performing analog signed weight multiplications to compute the dot-products required for self-attention. We implement Sliding Window Attention, which keeps memory of a finite set of past steps. A charge-to-pulse converter for array readout eliminates the need for analog-to-digital conversion between self-attention stages. Using a co-designed initialization algorithm to adapt pre-trained weights to gain cell non-idealities, we achieve NLP performance comparable to ChatGPT-2 with minimal training iterations, despite hardware constraints. Our end-to-end hardware design includes digital controls, estimating area, latency, and energy. The system reduces attention latency by up to two orders of magnitude and energy consumption by up to five orders compared to GPUs, marking a significant step toward ultra-fast, low-power sequence generation in Large Language Models.

1. Introduction

Transformer networks [1] are today’s state-of-the-art neural networks for sequence processing, outperforming both Convolutional Neural Networks (CNNs) and Recurrent Neural Networks (RNNs). The success of Transformers relies on the attention mechanism [2] to identify temporal correlations. Unlike RNNs, which build an implicit

memory through temporal dependencies of neuron states, the attention mechanism uses an explicit memory by comparing each sequence element, known as a token, with elements from many time steps simultaneously. This explicit memory mitigates the vanishing/exploding gradient problem during backpropagation through time present in RNNs. Comparisons between tokens are made using dot-products between different projections of the input sequence, called queries (Q), keys (K), and values (V) as illustrated in Figure 1 (a).

For generative tasks, the best performances are achieved by auto-regressive, decoder-only Transformers. At each inference step, the decoder generates a token, which is then appended to the input sequence, forming the input for the subsequent step. In a single decoder inference step, the attention mechanism uses only the Q projection of the current token. However, it must compute the dot-products with K and V projections of all previously generated tokens. To avoid re-computation of K and V during text generation, the KV-caching method stores the projections from previous tokens in memory and updates the KV-cache with the new projections.

For each token, the Graphical Processing Unit (GPU) must transfer the entire KV-cache from its High Bandwidth Memory (HBM) to its SRAM memory. Additionally, the KV-cache is often much larger than the SRAM memory due to the dimensions of the stored projections and the sequence length [3]. For instance, the entire KV-cache of the model Mistral 7 B [4] requires 8 Gb for a batch size of one. In recent technologies, the data access energy requires higher energy than the computations [5]. Loading the projections K and V in the attention mechanism is thus a major bottleneck, causing increased energy consumption and latency in LLMs [6]. Hence, In-Memory-Computing (IMC) is an attractive alternative for energy-efficient transformer computation. Recent research publications proposed emerging non-volatile memory-based IMC architecture for Transformer inference [7, 8]. However, computing attention with these memory technologies presents challenges, as each inference step involves writing the K and V values. Non-volatile memory technologies, exhibit slow write speeds, high energy consumption during the writing process, and low endurance, which collectively limit their suitability for IMC of the attention mechanisms [9]. The authors of [10] proposed to employ FeFET-based IMC only for computing the linear projections of the transformer (i.e. converting input to Q , K , and V). The dot-product required for attention is computed in this work using CMOS units and SRAM-based memories are used to cache K and V . The same authors also used FeFET as fixed attention scores for memory-augmented neural networks [11]. Hence, there is a lack of IMC architectures that are capable of efficiently computing the attention operation of the transformer.

In this work, we propose a novel hardware architecture for attention computation, which is based on IMC with analog, capacitor-based gain cells performing signed weight Multiply-Accumulate (MAC) operations. First, our architecture eliminates the data write issues because gain cells have more endurance and require less write energy and time than non-volatile memories. Furthermore, since each gain cell is signed and multi-level, our architecture leads to a lower area footprint than an SRAM-

based implementation, as SRAMs require multiple cells to achieve multi-level precision. Moreover, SRAMs are fully volatile while gain cells can hold a state for up to multiple seconds. Our architecture computes the attention (i.e. two consecutive dot-products, scaling, and nonlinear activation function) entirely in the analog domain without converting to digital at any intermediate step, thus avoiding power and area-hungry Analog to Digital Converters (ADCs). We utilize Pulse-Width Modulation (PWM) to transmit analog signals between consecutive dot-products and to implement scaling and nonlinearity. We only use digital blocks to compute the final attention output using digital adders. Another key contribution of this work is a comprehensive analysis of Algorithm-Hardware co-optimization. First, we implement the Sliding Window Attention mechanism [12], which is adapted to IMC. Unlike conventional attention whose memory requirement scales with the sequence length, the Sliding Window Attention only keeps track of the most recent tokens. Second, we model hardware constraints and non-idealities and integrate them into the training process. Since training LLMs from scratch is extremely expensive and because the non-idealities do not permit direct model fine-tuning, we introduce an innovative adaptation algorithm. The algorithm scales each layer according to its statistics to adapt the model to the hardware characteristics. With our adaptation algorithm, our model reaches similar accuracy as a pre-trained Chat-GPT2 model with very few training iterations.

Our architecture achieves up to five and two orders of magnitude lower energy consumption and latency, respectively, in comparison to GPUs. We present chip-level implementation results, including a detailed floor plan and layout of all units. Overall, this work provides an in-depth Algorithm-Hardware analysis and co-design for IMC based attention computations.

2. Related work

2.1. Analog In-Memory-Computing with Gain Cells

In-memory Computing aims to mitigate memory access bottlenecks by performing computation directly within memory crossbar arrays [9]. These crossbar arrays are often based on non-volatile memories, such as memristive devices, Flash and FeFETs. However, in this context, few reports exist on using dynamic, easily writable technologies. Currently, the two dominant types of dynamic memory are SRAM and DRAM. While SRAMs have substantial area requirements and face challenges in implementing multi-bit weights [13], DRAMs are restricted to digital computations at the memory bank peripheries due to destructive read operations, preventing parallel reads across the entire array [14,15]. In this context, gain cells are a potential alternative to commodity DRAM [16]. Unlike DRAMs, gain cells accumulate current on bit lines and are compatible with CMOS, enabling flexible integration. Similarly to DRAM, gain cells feature a capacitor to store information in charge. These cells offer substantial advantages over traditional DRAM by incorporating a second transistor within the read

path (2T1C), with its gate connected to the storage capacitor. This second transistor allows for a non-destructive read: instead of reading directly the capacitor’s charge, this read transistor implements a high-gain path from small charge variations at the gate to large variations of output currents. For applications such as digital storage devices, this design allows for much smaller capacitance due to the high gain, even eliminating the need for a separate physical storage capacitor, only using the transistor’s gate capacitance instead, resulting in a 2T0C configuration. Typically, these gain cells write transistors are implemented using oxide-based transistors like Indium Gallium Zinc Oxide (IGZO), which offers very low leakage currents resulting in retention times in the order of multiple seconds [17, 18]. In this context, hybrid systems are used to implement the write and read paths separately, with the write path in IGZO technology and the read path in standard silicon CMOS. This is enabled by the CMOS compatibility of IGZO technology. This configuration offers much higher gain and better reliability while enabling long retention times and non-destructive readouts. The potential of gain cells for IMC was demonstrated in [19, 20], where the authors have shown that they can successfully perform analog dot product operations in memory. Here, the read transistors perform the multiplication from the voltage to the current domain. Due to the inherent non-linear characteristics of transistors, a linearization step is required for this process [21]. Recently, more advanced gain cell-based multiplier structures that push either positive or negative current onto the bit line have been developed, enabling signed weight multiplications [22]. Our circuit shares similarities, but it is adapted for standard CMOS processes, whereas [22] is adapted to the FD-SOI CMOS process. In [23], a Voltage-to-Time Converter with Rectified Linear Unit (ReLU) characteristics was introduced for integration with the multiplier cell from [22]. In our work, we utilize two variants of this cell: the original saturated ReLU version as proposed, and a modified version featuring linear characteristics, capable of producing signed outputs.

2.2. Hardware Attention

Most Transformer attention inference today is performed on either GPUs or TPUs. Multiple approaches for Transformer accelerators in hardware have been proposed. Most literature can be found regarding specialized digital ASICs for Inference [24] or by reducing the amount of computation through various pruning algorithms, [10, 25]. In one approach [26], DRAM arrays are used to store the KV matrices, while performing MAC operations at the periphery of the memory banks. However, this method does not offer full parallelism.

More advanced analog IMC techniques have also been proposed, leveraging FeFET for in-memory linear projection computations and utilizing CMOS-based crossbars as cache to store attention scores for future reuse. Notably, in this method, the attention itself is not computed in memory [10]. This contrasts with our approach, which explicitly aims to compute the attention within the KV cache. In another work [27], the projections are computed using memristor crossbar arrays, while SRAM is employed to

perform in-memory attention computations. Because this architecture requires loading multiple queries at once in SRAMs, this approach is not adapted to auto-regressive Transformers where only one query can be accessed at a time. However, this approach results in a larger area footprint and lacks the capability for signed and multilevel weights within the multiplier cells.

Some works have attempted to exploit the parallelism of memristor crossbar arrays for computing the attention mechanism itself [7, 8]. However, computing attention using non-volatile devices is problematic due to the high programming energy, limited write endurance, and low write speeds in non-volatile resistive switching devices [9]. In contrast, our approach addresses the frequent write demands of the attention KV matrices by opting to use capacitor gain cells for the KV-cache, which also offers IMC capabilities.

3. System, Algorithm and Architecture

In this section, we describe the basics of the attention mechanism, followed by a detailed description of our analog IMC implementation, and the algorithm-hardware co-optimizations.

3.1. Attention Mechanism

In auto-regressive Transformers, each token is compared with the projections of past tokens stored using KV-caching. The weights $W_{Q,K,V} \in \mathbb{R}^{D,d}$ generate the queries, keys, and values from an input token $x_i \in \mathbb{R}^{1,D}$:

$$Q_i, K_i, V_i = W_{Q,K,V} x_i. \quad (1)$$

The keys and values $K_i \in \mathbb{R}^{1,d}$ and $V_i \in \mathbb{R}^{1,d}$ are stored as part of the full KV-cache with $K \in \mathbb{R}^{T,d}$ and $V \in \mathbb{R}^{T,d}$. The query $Q_i \in \mathbb{R}^{1,d}$ is not stored but used for inference as

$$S_i = Q_i \cdot K^T; \quad A_i = \phi \left(\frac{S_i}{\sqrt{d}} \right) \cdot V. \quad (2)$$

The dot product between the queries and keys produces an attention score matrix $S_i \in \mathbb{R}^{1,T}$. This attention score matrix is then scaled by the square root of the head dimension d and is typically passed through a softmax function to normalize the attention scores. However, other nonlinear activation functions ϕ can be used instead of softmax, yielding similar accuracy [28, 29]. The output of the attention mechanism A_i is then obtained by the dot product between the output of the nonlinear function $\phi(S_i)$ and the values. In multi-head attention, different heads are implemented in parallel with different projection weights. The results of the different attention heads are concatenated and another linear layer produces the final multi-head attention result.

In the full attention mechanism, the attention score matrix S compares all past, present, and future elements of the sequence. However, different types of attention are used in state-of-the-art large language models (LLMs). In causal attention, for instance,

a mask is applied to prevent each query element from attending to future elements. Another widely used form of attention is Sliding Window Attention [12], which utilizes only local information. For each input query, only the past keys and values M from the past are retained, and the others are masked (see Figure 2 (a)). Although Sliding Window Attention is local at each layer, it can still capture global information in deep networks because the receptive field grows with the number of layers [4]. This form of attention enables us to store the sequence in physical memory without requiring the storage of data scaling with the full sequence size.

LLMs generate text in an auto-regressive manner, which means that each generated token is fed as input to the network to generate the next token. In this context, the sequence is computed sequentially. Only one token $x \in \mathbb{R}^{1,D}$ is thus fed as the input of the attention mechanism for each time step. In this work, we implement a sequential Sliding Window Attention mechanism using a Rectified Linear Unit (ReLU) function for nonlinearity instead of softmax. This approach is more hardware-friendly, as the normalization operations required by softmax necessitate an additional vertical connection along the sequence dimension [30], which is typically very large and challenging to implement using analog circuitry.

We first show how a single gain cell can store information and operate a signed multiplication. Then we show how arrays of these gain cells can implement the two dot products required for the attention mechanism.

3.2. Gain cell-Based Signed Weight Multiply-And-Accumulate Operations

Figure 1(c) presents our proposed single multiplier cell, designed to perform the MAC operations in the attention accelerator. The cell contains a write stage to write the value of either Q or K to the stage capacitor C_1 , which acts as a memory, and a multiplication stage that approximates the product between the input and the stored weight.

The store stage capacitor is charged with a 15 ns multi-level voltage pulse emitted by a Digital to Analog Converter (DAC). The voltage pulse is gated to the designated capacitor by a write-enable (WE) transmission. The transmission gate enables discharging and charging the capacitor during write phases and operating non-destructive read phases.

The multiplication stage generates a current dependent on the stored capacitor voltage (V_{store}), which implements the weight as depicted in Figure 1 (e). The input, which is a PWM signal, controls the state (closed or open) of another transmission gate. The read path is arranged in a push-pull configuration consisting of two other transistors operating the multiplication. If V_{store} is close to V_{SS} , only the PMOS transistor will source current into the word line (WL), resulting in a positive output current. Conversely, if V_{store} is closer to V_{DD} , only the NMOS will conduct, drawing current out of the word line and resulting in a negative output. If the stored voltage lies between the supply voltages, the currents of both transistors will be small and cancel each other out, resulting in zero current output. Both multiplying transistors are sized

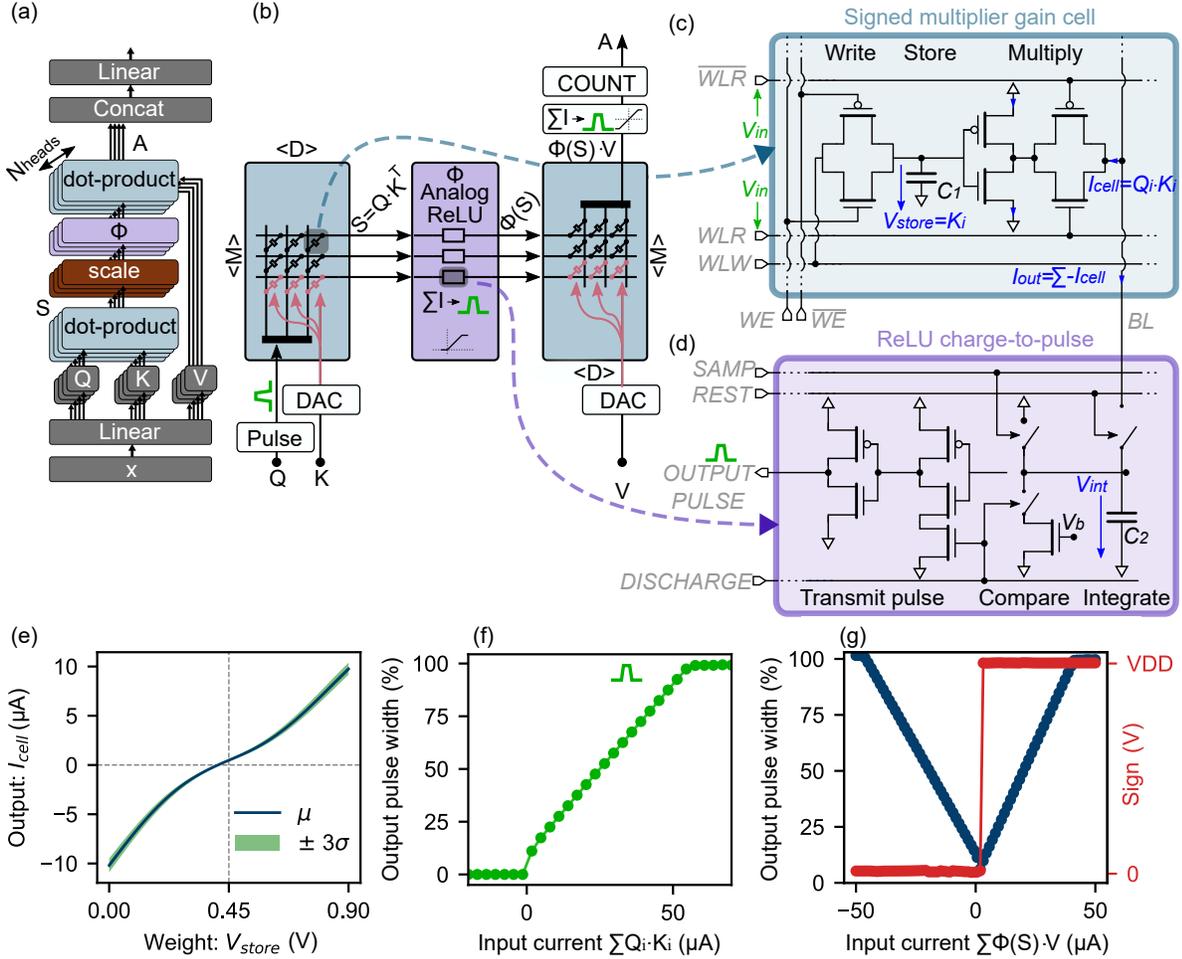


Figure 1. (a) Multi-head attention mechanism. (b) Hardware architecture of the attention inference accelerator. (c) Circuit diagram of a gain cell based signed weight multiplier cell used in the attention computation. (d) Diagram of the ReLU charge-to-pulse circuit. (e) Output current of gain cell based signed weight multiplier $i(W_{i,j})$ for different weight voltages V_{store} at a 'high' input, resulting in a signed output current, including CMOS process variations. (f) behavior of the ReLU charge-to-pulse circuit for different V_b . (g) The behavior of the signed charge-to-pulse circuit.

so that the positive and negative output currents are balanced. In Figure 1 (e), we show the relation between the output current and the voltage stored in the capacitor V_{store} with one cell simulated through SPICE simulations. We can see that this relationship is close to linearity within the operating range of the capacitor, but we will still consider nonlinearity for our experiments. This figure also highlights the expected variability of the generated current obtained by Monte Carlo simulations.

The input of the cell is encoded into voltage pulses with a variable duration between 0 ns and $T_{max} = 15$ ns. The pulses can be generated by 4 bit (16 levels) voltage pulse generators with 1 GHz clock signal. Because the transmission gate of the multiplication stage is driven by the voltages of the input word line (WLR and \overline{WLR}), the cell generates current only for the input pulse duration.

In an array of signed weight gain cells, multiple cells contribute currents to a shared

bit line (BL). According to Kirchhoff’s law, the total current on the bit line is the sum of the currents from all connected cells. For each inference step, the currents of the bit line are integrated for a duration corresponding to the maximum input pulse width T_{max} using an integration stage (see Figure 3 (d)). Therefore, the output of each bit line is the product of the input pulse duration with the generated currents, which depend on the stored weights.

3.3. Dot-Products and Nonlinear Activation Function with Analog Gain Cells Arrays and Analog Charge-to-Pulse Converters

The architecture of the proposed hardware attention mechanism is depicted in Figure 1 (b). Two arrays of analog gain cells implement the two dot products of the attention mechanism, while an intermediate charge-to-voltage pulse converter block converts the signal between the two arrays and implements a ReLU activation function. In this section, we will show how the inference is performed for a single input token $x \in \mathbb{R}^{1,D}$.

To implement the first dot-product ($Q_i \cdot K^T$), the columns are written with one column of the keys matrix $K \in \mathbb{R}^{M,d}$. The M columns of the array correspond to the keys of the previous M tokens, and the rows of the arrays correspond to the d different embedding elements. As explained in Section 3.2, the gain cells generate currents depending on their stored voltage which are summed along the bit lines.

The query $Q_i \in \mathbb{R}^{1,d}$ is encoded as input of the first gain cells array, through PWM voltage pulses. Therefore, the gain cell arrays outputs currents are also encoded temporally, and thus they need to be integrated to retrieve the correct MAC results. Moreover, the second array also requires voltage pulse width PWM input.

Rather than utilizing an operational amplifier integrator combined with ADCs, which are both space- and energy-consuming, the signal between the two arrays is converted by a circuit as depicted in Figure. 1 (d) that integrates the currents and emits a voltage pulse of variable width depending on the accumulated charge, similarly as in [22]. This charge-to-pulse circuit operates in three distinct phases: sampling, discharge, and reset. During the sampling phase, input pulses are applied to the first gain cell array, and the currents generated by the cells are integrated by a capacitor (C_2) in the charge-to-pulse circuit. This capacitor also utilizes the wire capacitance of the word line. In the discharge phase, the voltage of the capacitor C_2 is discharged with a constant current controlled by the bias voltage V_b . An inverter acts as a simple comparator, triggering a pulse of variable width. Finally, in the reset phase, the bit line is reset to the initial bit line voltage to prepare for a new inference step. The charge accumulated by the capacitor C_2 in the charge-to-pulse block at the end of each bit line is

$$S_i = \int_0^{T_{max}} I_i(t) = \sum_j Q_j \cdot i(K_{i,j}), \quad (3)$$

where $I_i(t)$ is the total current on the bit line, Q_j are the input pulse duration, and $i(K_{i,j})$ are the currents generated by the different cells when their transmission gate is closed, and depending on the charge of their capacitor $K_{i,j}$. The width of the pulse depending on the charge is presented in Figure 1 (f). The pulse is emitted only if the charge is positive, in accordance with the ReLU function. Then, the pulse width increases linearly with the charge, until it saturates to the maximum pulse width when the circuit reaches a threshold S_{sat} . This relationship can be modeled as

$$\phi(S) = \begin{cases} T_{max} & \text{if } S \geq S_{sat} \\ \frac{T_{max}}{S_{sat}} S & \text{if } 0 < S < S_{sat} , \\ 0 & \text{if } S \leq 0 \end{cases} \quad (4)$$

where $T_{max} = 15$ ns as for the input pulse generators.

The pulses representing $\phi(S) \in \mathbb{R}^M$ generated by the ReLU currents-to-pulse converters are fed to the word lines of the second gain cell arrays. The capacitors of these gain cells are charged with values corresponding to the values V . Therefore, the second gain cell array performs the dot product $\phi(S) \cdot V$, similarly as the first array implements the dot-product $Q \cdot K^T$. A different type of charge-to-pulse circuit integrates the output currents of the second array. Unlike the ReLU charge-to-pulse circuit, this design is a signed charge-to-pulse circuit, capable of generating pulses for both positive and negative input charges. This circuit features both charging and discharging paths. At the end of the sampling phase, a D-Flip Flop stores the result’s sign, which is determined by comparing $V_{int} < V_{DD}/2$. During the discharge phase, this sign determines whether the capacitor is charged (for a negative result) or discharged (for a positive result). Additional transmission gates ensure a consistent, high-active, width-modulated pulse at the block’s output. Moreover, this signed charge-to-pulse circuit outputs the sign stored in the D-Flip Flop. This relationship is illustrated in 1 (g). A digital counter measures the generated pulses’ width and multiplies the result by the retrieved sign bit, resulting in a total precision of 5 bits (16 negative levels and 16 positive levels).

We explained how the entire inference is performed to process one token using hardware dot-products and analog charge-to-pulse conversions implementing a non-linear activation function. Now, we show how this architecture can be used to process multiple tokens sequentially, implementing the Sliding Window Attention.

3.4. Hardware Sliding Window Attention with Online Write And Read Cycles

For Sliding Window Attention, the input query is multiplied only with the M most recent keys and values, corresponding to the window size M . At each time step, the keys and values must be updated with the most recent token and the oldest one must be forgotten. All others remain stationary until they are updated after M cycles. In our implementation, we write the array that encodes the keys and values at inference time in a column-wise manner. One important aspect to note is that the structure of the arrays containing K and V must differ from each other. In the K array, a

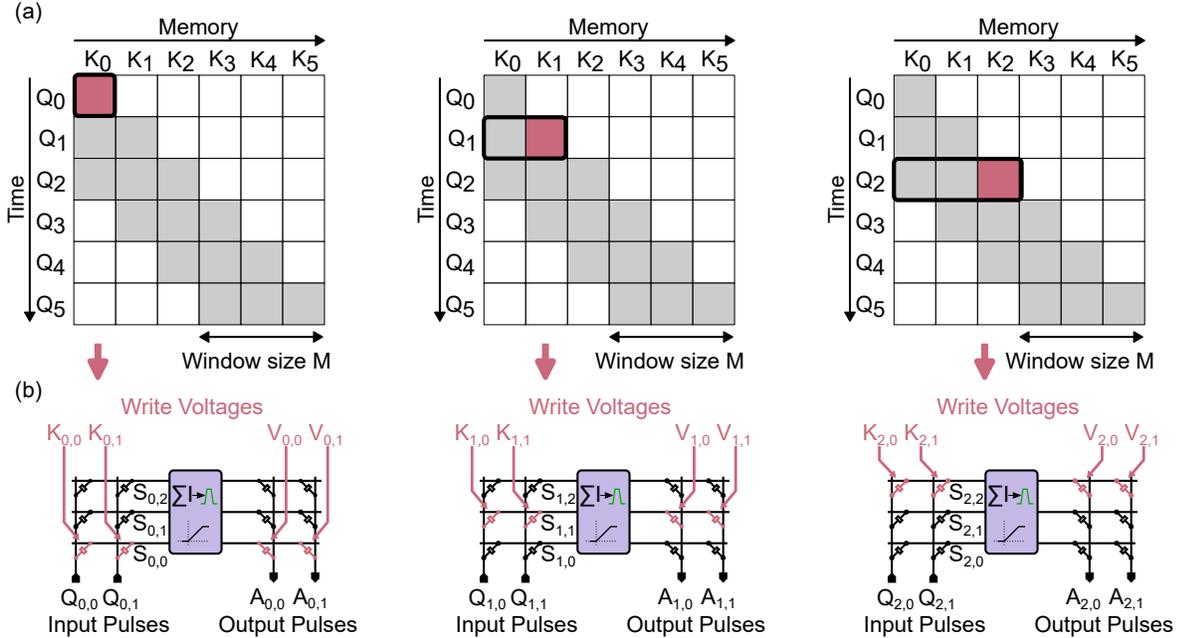


Figure 2. (a) Three inference steps of a dot-product between Q and K in Sliding Window Attention. The grey boxes represent tokens that are attended to, and the blank boxes the masked tokens. (b) Equivalent gain cell array implementations for an entire attention head. A new column of K and V is written before each inference step.

column corresponds to the input dimension, whereas in the V array, a row corresponds to the output dimension. Thus, the write enable signals of the V array are transposed compared to the ones of the K arrays (see Figure 2 (b)). At time step $t = 0$, we write the d cells of the first row using the vectors K_0 and V_0 , and we perform the attention computation with inputs Q_0 . At time step $t = 1$, we write the cells of the second row using the different K_1 and V_1 and repeat the attention computation with Q_1 . After M time steps, when all the rows of the array have been written, we overwrite the first row of the array, thus forgetting the oldest stored key. The succession of the different write and read cycles implements a sequential Sliding Window Attention.

3.5. Scaling to Large Dimension Hardware Attention Mechanism

IR drop, caused by resistive losses in interconnects, results in reduced accuracy in large-scale analog crossbar arrays [31]. To mitigate IR drop issues, we limit the size of our gain cell arrays to 64×64 . However, most Natural Language Processing (NLP) applications require larger dot-product dimensions within the attention head. Specifically, the memory of a Sliding Window Attention-based large language model (LLM) depends on its window size M . In our implementation, the sliding window size is determined by the number of columns, which is limited to 64 per array. Consequently, to accommodate larger window sizes and increase the model’s memory, we perform inference across multiple sub-tiles, each containing a different array.

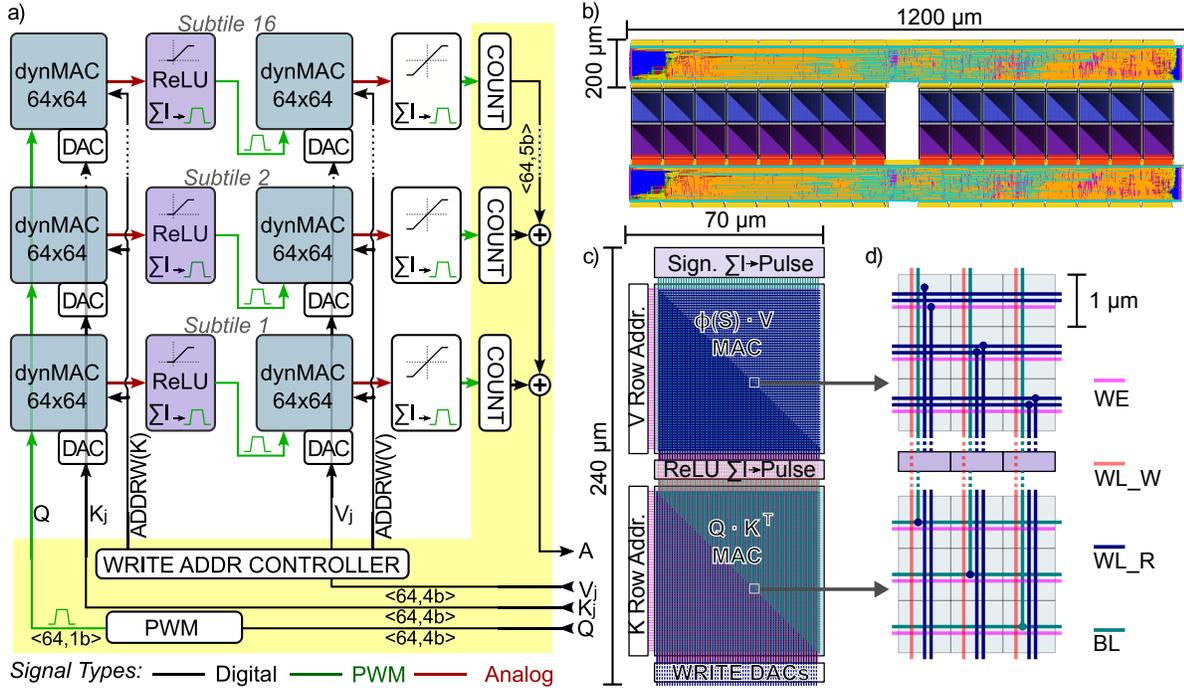


Figure 3. (a) Proposed hardware architecture for a single attention head, featuring the tiling of the attention head into multiple sub-tiles. The digital peripheral control is highlighted in yellow. (b) Layout floor plan of the architecture for one attention layer using IGZO technology assumptions. (c) Floor plan of one sub-tile. (d) Routing of one sub-tile highlighting the vertical propagation of signals by wire taping.

In this paper, we implement an Large Language Model (LLM) with an embedding dimension $d = 64$ and a sliding window size $M = 1024$. Therefore, we use 16 sub-tiles to perform the entire attention head. Each sub-tile consists of two dot-product arrays, an analog ReLU charge-to-pulse block, and a readout circuit including charge-to-pulse blocks and digital counters. All tiles receive the same input $Q \in \mathbb{R}^{1,d}$ in parallel, which is a PWM signal generated by the digital block. The gain cells of each sub-tile are written with K and V pairs corresponding to a fraction of the entire sliding window. For example, the cells in the first array of the first sub-tile store key addresses from K_0 to K_{63} , the second sub-tile stores key addresses from K_{64} to K_{127} , and so forth. A write address controller keeps track of the current write index. To obtain the final attention results, the outputs of the pulse counters are summed by 64 digital adders, each with 12 inputs.

3.6. Pre-trained Models Hardware-Aware Fine-Tuning

The substantial time and energy costs of training LLMs can hinder the on-chip deployment of hardware neural networks. It is thus essential to integrate our gain cell-based attention hardware into an LLM without retraining it from scratch. However, using pre-trained weights from existing models is challenging because our attention mechanism differs from the conventional ones. Indeed, the analog gain cell multiplier

does not perform ideal multiplications between the input and stored voltages, since the I-V curve is nonlinear (see Figure 1 (e)). Our architecture implements Sliding Window Attention instead of causal attention and uses a different nonlinear activation function than softmax. The input and output are quantized by the DACs and the ADCs. Finally, the capacitors' leakages induce decay in the stored values. As depicted in Figure 4, we present an algorithm enabling adaptation of the hardware constraints of our attention mechanism to the pre-trained models, facilitating fine-tuning with significantly fewer training steps compared to training from scratch.

Because the nonlinearity of the gain cells increase the training memory cost and reduces training stability, we first transfer the weights of a pre-trained model to an intermediate linear hardware model. This linear model already incorporates different hardware constraints and scaling to accurately represent the expected currents on the bit lines, but with linearized gain cells. To model the linear gain cells, we use the equation

$$z = \beta x (y - y_{offset}), \quad (5)$$

where z is the output current, x is the input voltage of the cell, y is the stored voltage, $y_{offset} \simeq 0.45$ V corresponds to $V_{dd}/2$, and β is a linear fit parameter from the curve in Figure 1. The capacitor leakage leads to each stored voltage to decay as

$$y(t) = y(0) e^{-\frac{t}{\tau}}. \quad (6)$$

In our simulation, we chose a time constant $\tau = 1$ s. In other work, time constant > 1 s were reported in gain cell memories [18,19]. After discretization of Equation (6), we can use the equation

$$y_t = y_{t-1} e^{-\frac{\Delta_t}{\tau}}, \quad (7)$$

where we chose $\Delta_t = 65$ ns to be equal to the latency of our full hardware attention mechanism (see Figure. 5.1 (a)). It is noteworthy that the decay of stored keys and values may not necessarily hinder network performance: several approaches in Deep Learning leverage exponential decay masks to enhance memory structure [29, 32, 33]. We use Equation 4 to model the charge-to-pulse circuits. We implement the Sliding Window Attention by masking the elements of S outside the sliding window (blank spaces in the example Figure 1). Because Q , K , V , and the final output are quantized, they are clipped between minimum and maximum values. The charge-to-pulse circuit outputs are also clipped between zero and maximum pulse width (see Equation 4). To avoid most values being saturated outside the clipping bounds, and to adapt the the nonlinear operation made by the gain cells, we introduce scaling operations defined as

$$y = ax + b \quad (8)$$

with two scalar training parameters a and b . We use this scaling operation, with independent parameters, before quantization of Q , K , V , and before the final output after digitization. Therefore, these scaling operation are done digitally and do not require extra analog hardware.

We fine-tune this linear model through backpropagation with Quantization Aware Training [34], which means that during training the quantization is done only in the forward pass and the backward pass is done in full precision. The quantization has 16 levels for the input PWM circuit, 8 levels for the stored capacitor voltages K and V , and 32 levels for the output DACs. Once our linear model reaches an accuracy equivalent to the original model (after 3000 iterations), we transfer the weights to the final model including the gain cell’s nonlinearity. To adapt the linear model to the nonlinear one, we initialize the scaling parameters a and b using an algorithm inspired by [35]. Given a set of input samples, we use an iterative loop that updates the scaling parameters so that the output of the scaling function of the nonlinear model matches the statistics of the linear model. At each iteration, we measure the standard deviation σ_L and the mean μ_L of the output of every scaling stage of the linear model (see Eq. 8), as well as the standard deviation σ_{NL} and the mean μ_{NL} of the output of every scaling stage of the nonlinear model. We update the scaling parameters a and b of the nonlinear model as

$$\begin{aligned} a &\leftarrow a \frac{\sigma_L}{\sigma_{NL}} \\ b &\leftarrow b + (\mu_L - \mu_{NL}) \end{aligned} \quad (9)$$

We repeat the algorithm until the mean and standard deviation of the scaling functions output of the nonlinear model matches the mean and standard deviation of the linear model within a tolerance ratio. Finally, we fine-tuned the nonlinear model using backpropagation. The forward pass of the gain cell-based multiplication is done using a third-order polynomial fit modeling the I-V curve characteristics of the devices. For the backward path, we use only a linear fit which is less costly in computation and more stable. Previous work has demonstrated that incorporating the nonlinearity of physical systems during training can mitigate the accuracy degradation they cause [36,37].

4. Experimental Methods

4.1. Training algorithm

To evaluate our training algorithm and the inference accuracy of our architecture, we implemented the analog gain cell-based attention mechanism on the ChatGPT-2 architecture [38]. ChatGPT-2 is a Transformer neural network with 124 million parameters, 12 layers, an attention mechanism input dimension of 768, 12 heads per attention block, and a head dimension of 64. We used the open-source text collection OpenWebText [39] split between training and testing samples, and the pre-trained ChatGPT-2 tokenizer to encode the plain text into tokens (vectors of size 50,304 each). Each training iteration had a batch size of 480, with sequences of length 1024 per sample. We selected a sliding window size of 1024, which matches the number of gain cell rows in the memory. Since the sequence length also equals 1024, each gain cell is written only

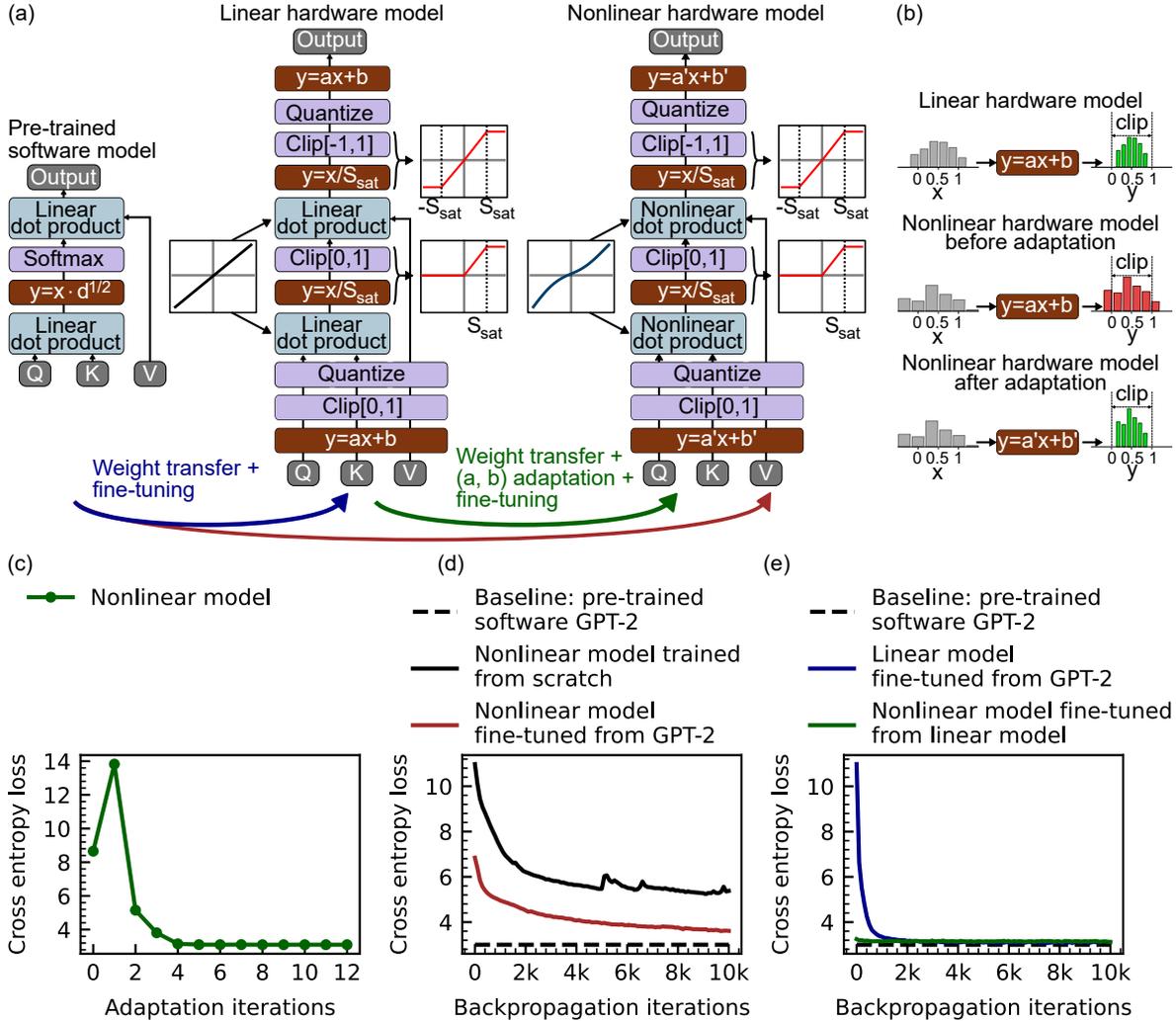


Figure 4. (a) Training algorithm. From a software pre-trained model, we fine-tune an intermediate model that integrates all hardware constraints except nonlinearity. Then, we use our custom initialization algorithm to adapt the gain cell’s nonlinearity to the intermediate model. Finally, we fine-tune the model by integrating the gain cell’s nonlinearity. (b) Sketch of the adaptation algorithm for scaling factors. Scaling factors re-scales the input before clipping and quantization. The nonlinear model leads to different statistics (red histogram) from the linear model (green histogram). The adaptation algorithm modifies the scaling factors so that the statistics of the nonlinear model matches the statistics of the linear one. (c) Evolution of the loss function during our adaptation algorithm, which leverages the linear model to initialize the scaling parameters a and b of the nonlinear model. (d) Nonlinear model training results without our adaptation algorithm. Training from scratch (black curve), and training from a pre-trained model (red curve). (e) Training results with our adaptation algorithm. We plot the training curve of the linear model (blue curve), and the nonlinear model (green curve) model fine-tuned from the linear model.

once per sequence, eliminating the need to overwrite cells during one sliding window iteration. For a larger sequence length, the gain cells would be overwritten, as described in Section 3.3. To train the network, the next token in the sequence is predicted for each

input token. Thus, the target sequences are the input sequences shifted by one token. The cost function used was cross-entropy, calculated between the predicted sequence and the target sequence. We used backpropagation with the AdamW optimizer [40], with a learning rate of 10^{-5} (except for the linear network, where we use a learning rate of 6.10^{-4}) and a weight decay of 0.1. The results of each evaluation are averaged over 1,000 samples.

4.2. Hardware SPICE simulations

To assess circuit performance accuracy, as well as values for energy consumption and speed, we conducted SPICE array simulations using the TSMC 28 nm PDK within the Cadence Virtuoso environment. All simulations are based on a 64×64 array, corresponding to the tile size in our architecture (see Figure 3 (a)). In these simulations, a parasitic wire capacitance of 0.8 fF and a series resistance of 2Ω per array element are included. Both arrays, one performing $\Phi(Q \cdot K^T)$ and the other performing $\Phi(S) \cdot V$, are simulated separately, but always in combination with their specific charge-to-pulse circuitry readout circuitry.

4.3. GPU Attention inference energy and latency for comparison

To compare the computing speed and energy consumption of our architecture with existing technologies, we measured the latency and power consumption of two GPUs. One is a consumer Nvidia RTX 4090 GPU, and the other is a Nvidia Jetson Nano, which is designed for embedded applications. We perform ten runs of 1024 steps of auto-regressive token generation with a twelve attention heads. For a fair comparison, the linear projections are not implemented in this experiment since they are also not implemented by our hardware architecture, and the static power (measured before inference) is subtracted from the power measured during inference. For each run, we measure the latency and the power using the Nvidia-SMI python API, and average them.

4.4. Speed and Latency

Speed analysis was conducted using SPICE simulations to evaluate a realistic operation speed. Since we are using an auto-regressive transformer we only evaluate the elapsed time from presenting an input token to the point where an attention result A can be provided to the subsequent part of the transformer. We then examine the behavior of transient simulations, followed by comparing the attention scores computed on hardware with those used in our model.

4.5. Hardware Energy consumption

The values for Q , K , $\Phi(S)$, and V , which are inputs to our SPICE simulations were sampled from the distributions of the trained model, thus ensuring realistic estimations

for hardware inference. We provide the energy estimation for an entire attention head processing one token. The routing-related power consumption, resulting from tiling, is accounted for in the digital block. The energy estimations for the digital block (see Figure 3 (a)) were also obtained using TSMC’s 28 nm CMOS technology. The digital block was implemented in SystemVerilog, and Synopsys tools were employed for the synthesis, place, and route of the digital block. A propagated power analysis with 50 % switching activity was used to calculate the power consumption of the digital block. These estimates are based on the typical-typical (TT) process corner, operating at 0.9 V and 85 °C. To estimate the power consumption of the DAC, we again perform SPICE simulations including the driver circuitry. We then multiply the simulated power consumption by 128 (64 values written for the K and 64 for the V).

4.6. Area Estimation

To estimate the area of our design, we employ two complementary approaches. First, we provide an accurate measurement of the actual area occupied by our silicon CMOS demonstrator based on the TSMC 28 nm technology implemented gain cell array. Secondly, we will provide a custom floor plan with estimations derived from the literature concerning IGZO gain cells.

The pure silicon-based multiplier cell array incorporates Metal-on-Metal (MoM) capacitors, which are essential to the design and must be relatively large due to the high leakage associated with silicon transistors. The area estimation is derived from the physical layout and silicon implementation of CMOS technology, providing a precise representation of the space requirements. We performed the layout for this technology to accurately estimate the area of a single tile. Secondly, we present a custom floor plan specifically designed for an IGZO gain cell implementation to reduce the area footprint of our design. Indeed, larger retention times can be achieved with smaller gain cells since IGZO transistors have smaller leakage than silicon CMOS transistors and thus require smaller capacitance. This floor plan is based on assumptions from relevant literature [41], where IGZO gain cell arrays are noted for their ability to perform accurate dot-product operations. We assume a cell dimension of $1 \mu\text{m} \times 1 \mu\text{m}$, with all previously mentioned parameters remaining unchanged. This approach is supported by the reported compatibility of IGZO with existing CMOS processes [41]. In this floor plan, we also include the digital circuitry and routing, as illustrated in Figure 3 (b), to provide a projected view of the full-scale chip layout.

5. Results

5.1. Training Results

We train the linear model described in Section 3.6 on 3000 iterations with backpropagation and then we apply our adaptation algorithm to the hardware model (which includes the gain cells nonlinearity). In Figure. 4 (b), we show the evolution of

the cross-entropy loss with the number of adaptation algorithm iteration loops. We see that with only 12 iterations the hardware model already reaches a cross-entropy loss of 3.2, whereas the loss is 8.6 when we simply transfer the weight from the linear model to the nonlinear model. In Figure 4 (c, d), we compare the training procedure using the linear model with the results of training from scratch and training from a pre-trained model without intermediate step. After 10,000 iterations, the model trained from scratch (black curve) and the model fine-tuned from ChatGPT-2 (red curve) respectively reach a cross-entropy of 5.3 and 3.6. The linear model is fine-tuned from ChatGPT-2 (blue curve) and the hardware model is fine-tuned from the linear model (green curve). The hardware model only takes 500 iterations to reach a cross-entropy of 3.1. In comparison, the trained software ChatGPT-2 model has a cross-entropy of 3.0. We also fine-tuned a software ChatGPT-2 model with the same level of quantization as our hardware model and QAT. The quantized ChatGPT-2 reaches a cross-entropy of 3.1. In conclusion, our adaptation algorithm allows us to train a gain cell-based network with fewer training iterations than training from scratch, and an accuracy equivalent to software attention.

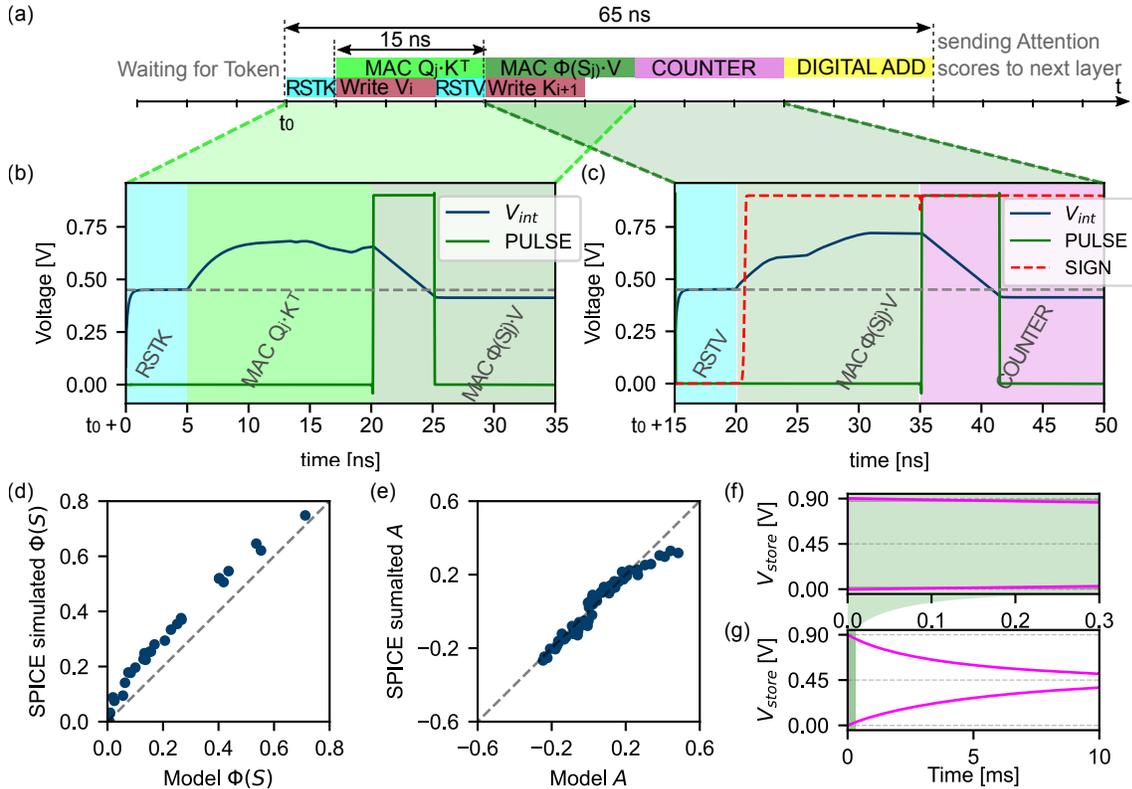


Figure 5. (a) Proposed pipe-lining, highlighting parallel operations of writing new KV values and performing the MAC operations. (b) Transient Simulation of the $\Phi(Q \cdot K^T)$ MAC operation including with indicated temporal location. (c) Transient Simulation results of the $\Phi(S) \cdot V$ MAC operation including the pulses and sign signal for the counter within the pipeline. (d) Comparison of expected results model versus Spice simulation results for the $\Phi(Q \cdot K^T)$ operation. (e) Comparison of PyTorch model versus SPICE simulation results for the $\Phi(S) \cdot V$ operation.(f) Silicon CMOS Capacitor Leakage over time within two different timescales.

Table 1. Downstream task results. acc measures the percentage of accurate word predictions, and ppl measure the perplexity, which measures the uncertainty of the prediction. * Publicly available Chat-GPT2 model. † Chat-GPT2 model trained from scratch.

	ARC-E	ARC-C	WinoGrande	HellaSwag	LAMBADA	LAMBADA	PIQA
	acc ↑	acc ↑	acc ↑	acc ↑	ppl ↓	acc ↑	acc ↑
Software model*	43.81	22.70	51.62	31.14	40.06	32.56	62.89
Software model†	41.04	23.81	49.72	29.22	70.83	26.24	60.77
Linear hardware model	41.46	22.53	50.59	28.83	82.80	21.77	61.64
Nonlinear hardware model	41.84	23.55	50.67	29.40	71.68	22.94	61.53

5.2. Downstream Task Benchmarks

To demonstrate the efficacy of the overall model architecture and fine-tuning approach, Table 1 shows the performance of several variations of our model and baseline models on standard language model bench-marking tasks. We evaluate four models that are increasingly true to the hardware implementation. The datasets cover various types of problems. Our bench-marking setup follows [42] and [43] in terms of evaluated tasks and metrics. ARC-Easy and ARC-Challenge [44] focus on question answering, with ARC-Easy containing straightforward questions and ARC-Challenge featuring more difficult ones. WinoGrande [45] evaluates commonsense reasoning and coreference resolution by presenting minimal pairs to resolve ambiguities. HellaSwag [46] tests commonsense inference, requiring models to predict the most plausible continuation of a given context. LAMBADA [47] evaluates models’ text understanding through a word prediction task that requires comprehension of broader discourse, not just local context. PIQA [48] assesses physical commonsense reasoning, testing a model’s understanding of physical scenarios.

Our nonlinear hardware model achieves a precision comparable to the one achieved by the public Chat-GPT2 model, except for the LAMBADA task. This is due to a reproducibility issue, as our Chat-GPT2 model trained from scratch also do not match the public Chat-GPT2 model. However, our model achieves a precision equivalent to our Chat-GPT2 model trained from scratch, which highlights that our hardware constraints do not hinder model training and accuracy.

5.3. Circuit Computing accuracy

The accuracy of an attention head, including the readout circuitry, is highlighted in Fig. 5.1 (d and e), where the same timing is used as described in Section 5.4. This is demonstrated for a single sub-tile, with two arrays representing both MAC arrays: one array containing the keys, incorporating the ReLU charge-to-pulse circuitry, and the other array containing the values, utilizing the signed charge-to-pulse circuitry (see Figure 4 (a)). The results from Fig. 5.1 (d) are used as the inputs for Fig. 5.1 (e). The circuit results are compared to the results of the attention model. The key difference between the model’s attention mechanism and the hardware implementation

is that, unlike the ideal current generators assumed in the model, gain cells exhibit non-ideal behavior. This discrepancy can be mitigated through further fine-tuning and optimization of the charge-to-pulse readout circuits.

5.4. Speed and Latency

Figure 5.1 (a) illustrates that a total time of 65 ns is required from the input query to the corresponding attention result. When the previous part of the transformer provides a new token, the process begins by computing the values $\Phi(S)$. Note that writing can be performed in parallel with the dot product operation, as when one array is computing, the other can be overwritten, and vice versa. The corresponding transient simulation for a single WL (Word Line) of the first array is displayed in Figure 5.1 (a). The process begins with a 5 ns reset of the WL (RSTK), followed by 15 ns for applying the input pulses to perform the dot product, and then a 15 ns discharge period to generate the output pulses for the second dot-product array. Figure 5.1 (c) presents the transient simulation results for this second dot-product array, which incorporates the signed pulse-to-charge circuitry. Similar to the previous stage, a reset (RSTV) is required, followed by applying the inputs from the preceding charge-to-pulse ReLU circuit to perform the dot product, which takes 15 ns. Afterward, a 15 ns discharge phase is required for the signed charge-to-pulse circuit, during which a digital counter simultaneously measures the pulse width and detects the sign. In the final step, estimated to take 15 ns, the results from each sub-tile are summed in the digital domain as indicated in Figure 5.1 (a), after which the final attention result, A , can be utilized by the next stage of the auto-regressive transformer.

5.5. Energy Consumption

In total, the MAC arrays within the attention head and the ReLU charge-to-pulse circuit which realize the $\Phi(Q \cdot K^T)$ operation, consume 1120 pJ per token computation. The arrays, which implement $\Phi(S) \cdot V$ and the signed charge-to-pulse circuitry consume 700 pJ. The lower energy consumption in the second dot-product arrays is attributed to the significantly sparser activation of $\Phi(S)$. Indeed, the zero voltage input does not produce currents in the gain cells and therefore reduces the power consumption. The digital control and routing block consumes a total power of 113.7 mW. Assuming total compute time of 65 ns, the estimated energy consumption is 4 nJ. The DAC’s in one head including drivers require 330 pJ per token. Overall we can estimate the power consumption of processing one token for one attention head to 6.1 nJ.

The energy and speed comparison between GPUs and our architecture are shown in Figure. 6 (a and b). Focusing on the attention mechanism alone, our architecture can lead to a speedup of $\times 7,000$ compared to Jetson Nano and $\times 300$ compared to RTX 4090, as well as an energy reduction of $\times 40,000$ compared to Jetson Nano and $\times 90,000$ compared to RTX 4090.

5.6. Retention Time and Weight decay

Due to leakage in the storage capacitors, the voltages gradually decay over time, leading to exponential changes in the weights of the dot-product matrices. This simulation is based on silicon CMOS technology. Figure 5.1 (f and g) presents the simulated transient response of the storage capacitor voltage V_{store} , which corresponds to the cells weight for both extreme values 0 V and 0.9 V. Figure 5.1 (f) highlights a stable operating window of 300 μ s, where the maximum weight decay is below 7%. Figure 5.1 (g) highlights the long-term exponential decay as well as the final relaxation state. Since gain cells do not generate current for V_{stored} value of 0.45 V, they decay toward a resting position with value 0. Therefore, we avoid undesired biases and power consumption increases for unwritten memories. Note that retention times using IGZO technology exceed silicon CMOS retention times by multiple orders of magnitude.

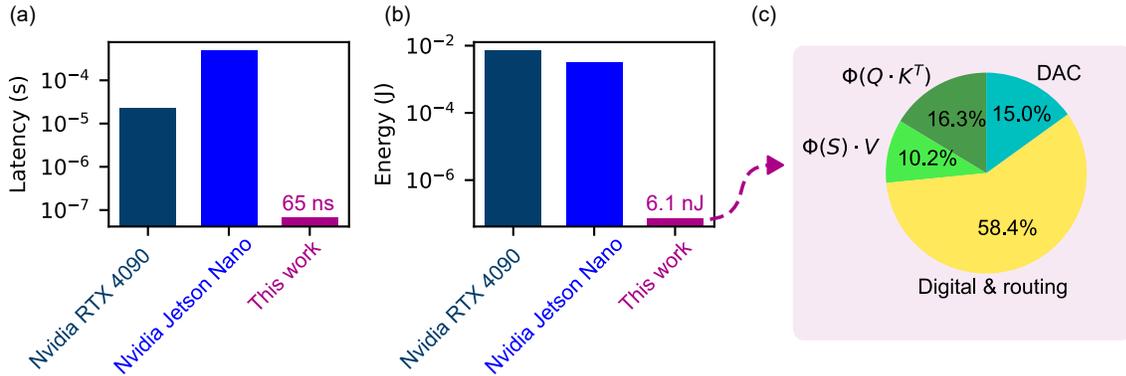


Figure 6. (a) Latency of the attention mechanism for one processed token and (b) energy consumption for a twelve head attention mechanism implemented by a consumer GPU, an embedded application-specific GPU, and our hardware architecture. (c) Energy consumption ratio for the different modules of our hardware architecture, including analog and digital signals.

5.7. Area and Floor plan

5.7.1. Silicon CMOS Area The CMOS demonstrator cell dimensions are primarily dictated by the MoM capacitor. However, all silicon components can be placed on a parallel layer. A single cell has dimensions of $3.9 \mu\text{m} \times 4.9 \mu\text{m}$. For a full 64×64 array, this results in a total area of 0.08 mm^2 per array. This calculation applies to both arrays. The ReLU charge-to-pulse circuitry occupies an area of 0.01 mm^2 , while the signed charge-to-pulse circuitry occupies around 0.02 mm^2 . The area of the charge-to-pulse circuits is dominated by the integration capacitors.

5.7.2. IGZO technology Area Our floor plan, incorporating IGZO assumptions, is presented in Figure 3 (b). The figure illustrates the arrangement of 16 sub-tiles for one attention head, alongside the digital circuitry. This structure is designed to be

vertically repetitive, allowing multiple attention heads to be efficiently integrated on a single chip. Each attention head receives inputs from the lower digital block, while its outputs are processed by the upper digital block. It is important to note that all attention heads on the chip will still operate in parallel to perform multi-head attention. We estimate the area of one head to be approximately 0.5 mm^2 . In Figure 3 (c), we show the floor plan of a single tile, which includes 64 shared DACs for writing the weights, two row address decoders, and the charge-to-pulse circuitry. To facilitate vertical signal propagation, we employ wiretapping, as highlighted in Figure 3 (d).

6. Discussion

The energy and latency reductions we predict compared to GPUs arise from several factors. Performing multiplications in the analog domain is inherently more energy-efficient and faster than digital computation. Writing values to gain cells consumes less energy than to non-volatile memories. Furthermore, due to the Sliding Window method, each value is written only once, unlike other In-Memory Computing gain cell methods [19] that require multiple refresh operations.

In our design, we deliberately avoid using power-hungry ADCs by using analog charge-to-pulse converters instead, resulting in a slight discrepancy between the obtained outcomes and the ideal attention model. Future circuit improvements and modeling are needed to further close this gap.

In our design, we opted for a conservative approach by implementing an IGZO gain cell with an area of $1 \text{ }\mu\text{m}^2$ per memory unit cell. The memory unit cell area is the limiting factor in the area footprint of our design. However, gain cell designs based on 2D materials are still an active area of research. In the future, smaller memory unit cells could be used, further decreasing the overall area footprint.

Although this study is limited to device simulations, the algorithm is designed to adapt to varying device characteristics, making it valuable for training hardware-based networks with real device inference.

The energy and speed improvements of our method focus on the attention mechanism, a major bottleneck in Deep Neural Network inference. However, to achieve significant reductions in the overall energy consumption of artificial intelligence systems, all components must be optimized. Our hardware attention mechanism can be integrated with other IMC techniques implementing low-power linear layers in deep neural networks.

7. Conclusion

In this paper, we tackle the challenges of latency and energy consumption in data transfer and computation within the attention mechanism of generative models. We have presented a novel analog In-Memory Computing (IMC) architecture, utilizing capacitor-based gain cells to effectively address these issues. We have demonstrated

that the entire attention computation can be executed using analog signals, with gain cell arrays performing the dot-products and analog pulse generators implementing the nonlinear activation functions. Our study presents a comprehensive end-to-end design of a hardware attention mechanism, integrating analog circuits for both memory and computation, alongside digital readout and input circuits. Our SPICE simulations demonstrate that the analog circuits can perform operations with high accuracy, and our neural network simulations confirm that a Large Language Model (LLM) implemented with these circuits can achieve text processing results comparable to software-based networks. Additionally, our weights adaptation algorithm significantly reduces the training time required for fine-tuning the hardware network, facilitating rapid chip deployment. Our architecture achieves a reduction in latency by up to two orders of magnitude and energy consumption by up to five orders of magnitude for attention computation. Overall, this work underscores the strong benefits of using In-Memory Computing with volatile yet low-power memories in attention-based neural networks, marking a critical step toward ultra-fast, low-power generative AI.

Acknowledgments

This work was supported in part by the Federal Ministry of Education and Research (BMBF, Germany) in the project NEUROTEC II (Project number: 16ME0398K). This work is based on the Jülich Aachen Research Alliance (JARA-FIT) at Forschungszentrum Jülich GmbH, Jülich, Germany.

The authors gratefully acknowledge the Gauss Centre for Supercomputing e.V. (www.gauss-centre.eu) for funding this project by providing computing time through the John von Neumann Institute for Computing (NIC) on the GCS Supercomputer JUWELS at Jülich Supercomputing Centre (JSC).

References

- [1] Vaswani A, Shazeer N, Parmar N, Uszkoreit J, Jones L, Gomez A N, Kaiser L and Polosukhin I 2023 Attention is all you need (*Preprint* 1706.03762) URL <https://arxiv.org/abs/1706.03762>
- [2] Bahdanau D, Cho K and Bengio Y 2016 Neural Machine Translation by Jointly Learning to Align and Translate arXiv:1409.0473 [cs, stat] URL <http://arxiv.org/abs/1409.0473>
- [3] Liu Z, Yuan J, Jin H, Zhong S, Xu Z, Braverman V, Chen B and Hu X 2023 arXiv:2402.02750 [cs] URL <http://arxiv.org/abs/2402.02750>
- [4] Jiang A Q, Sablayrolles A, Mensch A, Bamford C, Chaplot D S, Casas D d l, Bressand F, Lengyel G, Lample G, Saulnier L, Lavaud L R, Lachaux M A, Stock P, Scao T L, Lavril T, Wang T, Lacroix T and Sayed W E 2023 Mistral 7B arXiv:2310.06825 [cs] URL <http://arxiv.org/abs/2310.06825>
- [5] Jouppi N P, Hyun Yoon D, Ashcraft M, Gottscho M, Jablin T B, Kurian G, Laudon J, Li S, Ma P, Ma X, Norrie T, Patil N, Prasad S, Young C, Zhou Z and Patterson D 2021 Ten Lessons From Three Generations Shaped Google’s TPUv4i : Industrial Product *2021 ACM/IEEE 48th Annual International Symposium on Computer Architecture (ISCA)* (Valencia, Spain: IEEE) pp 1–14 ISBN 978-1-66543-333-4 URL <https://ieeexplore.ieee.org/document/9499913/>

- [6] Fu Y 2024 Challenges in deploying long-context transformers: A theoretical peak performance analysis (*Preprint* 2405.08944) URL <https://arxiv.org/abs/2405.08944>
- [7] Bhattacharjee A, Moitra A and Panda P 2024 *arXiv preprint arXiv:2402.02586*
- [8] Yang X, Yan B, Li H and Chen Y 2020 Retransformer: Reram-based processing-in-memory architecture for transformer acceleration *Proceedings of the 39th International Conference on Computer-Aided Design ICCAD '20* (New York, NY, USA: Association for Computing Machinery) ISBN 9781450380263 URL <https://doi.org/10.1145/3400302.3415640>
- [9] Sebastian A, Le Gallo M, Khaddam-Aljameh R and Eleftheriou E 2020 *Nature nanotechnology* **15** 529–544
- [10] Laguna A F, Sharifi M M, Kazemi A, Yin X, Niemier M and Hu X S 2022 *Frontiers in Electronics* **3** ISSN 2673-5857 URL <https://www.frontiersin.org/articles/10.3389/felec.2022.847069>
- [11] Reis D, Laguna A F, Niemier M and Hu X S 2021 Attention-in-Memory for Few-Shot Learning with Configurable Ferroelectric FET Arrays *2021 26th Asia and South Pacific Design Automation Conference (ASP-DAC)* pp 49–54 iSSN: 2153-697X URL <https://ieeexplore.ieee.org/document/9371584/?arnumber=9371584>
- [12] Beltagy I, Peters M E and Cohan A 2020 Longformer: The Long-Document Transformer arXiv:2004.05150 [cs] URL <http://arxiv.org/abs/2004.05150>
- [13] Choi E J, Choi I, Jeon C, Yun G, Yi D, Ha S, Chang I J and Je M 2022 *IEEE Solid-State Circuits Letters* **5** 234–237
- [14] Kwon Y, Lee S, Lee J, Kwon S, Ryu J, Son J, Seongil O, Yu H, Lee H, Kim S, Cho Y, Kim J, Choi J, Shin H, Kim J, Phuah B, Kim H, Song M, Choi A, Kim D, Kim S, Kim E, Wang D, Kang S, Ro Y, Seo S, Song J, Youn J, Sohn K and Kim N 2021 25.4 a 20nm 6gb function-in-memory dram, based on hbm2 with a 1.2tflops programmable computing unit using bank-level parallelism, for machine learning applications *2021 IEEE International Solid-State Circuits Conference, ISSCC 2021 - Digest of Technical Papers* Digest of Technical Papers - IEEE International Solid-State Circuits Conference (United States: Institute of Electrical and Electronics Engineers Inc.) pp 350–352 publisher Copyright: © 2021 IEEE.; 2021 IEEE International Solid-State Circuits Conference, ISSCC 2021 ; Conference date: 13-02-2021 Through 22-02-2021
- [15] He M, Song C, Kim I, Jeong C, Kim S, Park I, Thottethodi M and Vijaykumar T N 2020 *2020 53rd Annual IEEE/ACM International Symposium on Microarchitecture (MICRO)* 372–385 URL <https://api.semanticscholar.org/CorpusID:222316976>
- [16] Lu A, Lee J, Kim T H, Karim M A U, Park R S, Simka H and Yu S 2024 *Nature Reviews Electrical Engineering* **1** 24–34
- [17] Shi M, Su Y, Tang J, Li Y, Du Y, An R, Li J, Li Y, Yao J, Hu R, He Y, Xi Y, Li Q, Qiu S, Zhang Q, Pan L, Gao B, Qian H and Wu H 3503 Counteractive coupling igzo/cnt hybrid 2t0c dram accelerating rram-based computing-in-memory via monolithic 3d integration for edge ai (IEEE)
- [18] Belmonte A, Kundu S, Subhechha S, Chasin A, Rassoul N, Dekkers H, Puliyalil H, Seidel F, Carolan P, Delhougne R and Kar G S 2023 Lowest ioff < 3×10⁻²¹ a/μm in capacitorless dram achieved by reactive ion etch of igzo-tft *2023 IEEE Symposium on VLSI Technology and Circuits (VLSI Technology and Circuits)* pp 1–2
- [19] Wang Y, Tang H, Xie Y, Chen X, Ma S, Sun Z, Sun Q, Chen L, Zhu H, Wan J, Xu Z, Zhang D W, Zhou P and Bao W 2021 *Nature Communications* **12**
- [20] Gou S, Wang Y, Dong X, Xu Z, Wang X, Sun Q, Xie Y, Zhou P and Bao W 2023 *National Science Open* **2** 20220071
- [21] Chen Z, Chen X and Gu J 2021 15.3 a 65nm 3t dynamic analog RAM-based computing-in-memory macro and CNN accelerator with retention enhancement, adaptive analog sparsity and 44tops/w system energy efficiency *2021 IEEE International Solid- State Circuits Conference (ISSCC)* (IEEE)
- [22] Nägele R, Finkbeiner J, Stadtlander V, Grözing M and Berroth M 2023 *IEEE Transactions on Circuits and Systems I: Regular Papers* **70** 3509–3521

- [23] Finkbeiner J, Nägele R, Grözing M and Berroth M 2022 Design of an energy efficient voltage-to-time converter with rectified linear unit characteristics for artificial neural networks *2022 20th IEEE Interregional NEWCAS Conference (NEWCAS)* pp 327–331
- [24] Ye W, Zhou X, Zhou J, Chen C and Li K 2023 *ACM Trans. Embed. Comput. Syst.* **22** ISSN 1539-9087 URL <https://doi.org/10.1145/3549937>
- [25] Ham T J, Lee Y, Seo S H, Kim S, Choi H, Jung S J and Lee J W 2021 Elsa: Hardware-software co-design for efficient, lightweight self-attention mechanism in neural networks *2021 ACM/IEEE 48th Annual International Symposium on Computer Architecture (ISCA)* pp 692–705
- [26] Wu Y, Wang Z, Lu W D, , of Electrical EngineeringComputer Science D, the University of Michigan and Arbor A 2310 Pim-gpt: A hybrid process-in-memory accelerator for autoregressive transformers
- [27] Sridharan S, Stevens J R, Roy K and Raghunathan A 2023 *IEEE Transactions on Very Large Scale Integration (VLSI) Systems* **31** 1223–1233
- [28] Katharopoulos A, Vyas A, Pappas N and Fleuret F 2020 Transformers are RNNs: Fast Autoregressive Transformers with Linear Attention arXiv:2006.16236 [cs, stat] URL <http://arxiv.org/abs/2006.16236>
- [29] Ma X, Zhou C, Kong X, He J, Gui L, Neubig G, May J and Zettlemoyer L 2023 Mega: Moving Average Equipped Gated Attention arXiv:2209.10655 [cs] URL <http://arxiv.org/abs/2209.10655>
- [30] Vatalaro M, Moposita T, Strangio S, Trojman L, Vladimirescu A, Lanuzza M and Crupi F 2021 *Electronics* **10** ISSN 2079-9292 URL <https://www.mdpi.com/2079-9292/10/9/1004>
- [31] Lepri N, Glukhov A, Mannocci P, Porzani M and Ielmini D 2024 *IEEE Transactions on Electron Devices* **71** 1900–1906
- [32] Press O, Smith N A and Lewis M 2022 Train Short, Test Long: Attention with Linear Biases Enables Input Length Extrapolation arXiv:2108.12409 [cs] URL <http://arxiv.org/abs/2108.12409>
- [33] Wang S and Xue B 2023 State-space Models with Layer-wise Nonlinearity are Universal Approximators with Exponential Decaying Memory arXiv:2309.13414 [cs, math] URL <http://arxiv.org/abs/2309.13414>
- [34] Jacob B, Kligys S, Chen B, Zhu M, Tang M, Howard A, Adam H and Kalenichenko D 2017 Quantization and Training of Neural Networks for Efficient Integer-Arithmetic-Only Inference arXiv:1712.05877 [cs, stat] URL <http://arxiv.org/abs/1712.05877>
- [35] Mishkin D and Matas J 2016 All you need is a good init arXiv:1511.06422 [cs] URL <http://arxiv.org/abs/1511.06422>
- [36] Dong Q, Sinangil M E, Erbagci B, Sun D, Khwa W S, Liao H J, Wang Y and Chang J 2020 15.3 A 351TOPS/W and 372.4GOPS Compute-in-Memory SRAM Macro in 7nm FinFET CMOS for Machine-Learning Applications *2020 IEEE International Solid- State Circuits Conference - (ISSCC)* (San Francisco, CA, USA: IEEE) pp 242–244 ISBN 978-1-72813-205-1 URL <https://ieeexplore.ieee.org/document/9062985/>
- [37] Leroux N, Marković D, Martin E, Petrisor T, Querlioz D, Mizrahi A and Grollier J 2021 *Physical Review Applied* **15** 034067 publisher: American Physical Society URL <https://link.aps.org/doi/10.1103/PhysRevApplied.15.034067>
- [38] Radford A, Wu J, Child R, Luan D, Amodei D and Sutskever I 2019
- [39] Gokaslan A and Cohen V 2019 Openwebtext corpus <http://Skylion007.github.io/OpenWebTextCorpus>
- [40] Loshchilov I and Hutter F 2019 Decoupled Weight Decay Regularization arXiv:1711.05101 [cs, math] URL <http://arxiv.org/abs/1711.05101>
- [41] Liu S, Jana K, Toprasertpong K, Chen J, Liang Z, Jiang Q, Wahid S, Qin S, Chen W C, Pop E and Wong H S P 2024 *IEEE Transactions on Electron Devices* **71** 3329–3335
- [42] Gu A and Dao T 2024 Mamba: Linear-time sequence modeling with selective state spaces (*Preprint* 2312.00752) URL <https://arxiv.org/abs/2312.00752>

- [43] Beck M, Pöppel K, Spanring M, Auer A, Prudnikova O, Kopp M, Klambauer G, Brandstetter J and Hochreiter S 2024 xlstm: Extended long short-term memory (*Preprint* 2405.04517) URL <https://arxiv.org/abs/2405.04517>
- [44] Clark P, Cowhey I, Etzioni O, Khot T, Sabharwal A, Schoenick C and Tafjord O 2018 *ArXiv abs/1803.05457*
- [45] Sakaguchi K, Bras R L, Bhagavatula C and Choi Y 2019 *arXiv preprint arXiv:1907.10641* URL <https://arxiv.org/abs/1907.10641>
- [46] Zellers R, Holtzman A, Bisk Y, Farhadi A and Choi Y 2019 Hellaswag: Can a machine really finish your sentence? *Proceedings of the 57th Annual Meeting of the Association for Computational Linguistics*
- [47] Paperno D, Kruszewski G, Lazaridou A, Pham Q N, Bernardi R, Pezzelle S, Baroni M, Boleda G and Fernández R 2016 The lambda dataset: Word prediction requiring a broad discourse context (*Preprint* 1606.06031) URL <https://arxiv.org/abs/1606.06031>
- [48] Bisk Y, Zellers R, Bras R L, Gao J and Choi Y 2020 Piqa: Reasoning about physical commonsense in natural language *Thirty-Fourth AAAI Conference on Artificial Intelligence*